



# JGR Atmospheres

## RESEARCH ARTICLE

10.1029/2018JD029832

### Key Points:

- The initiation of a squall line occurred when a set of intersecting gust fronts approached a quasi-stationary dryline
- Convection was initiated at the vertex regions along the scalloped pattern of the intersecting gust fronts
- Vertex regions of the intersecting gust fronts had greater magnitudes and larger vertical and horizontal extents of updrafts

### Correspondence to:

Z. Meng,  
zymeng@pku.edu.cn

### Citation:

Bai, L., Meng, Z., Huang, Y., Zhang, Y., Niu, S., & Su, T. (2019). Convection initiation resulting from the interaction between a quasi-stationary dryline and intersecting gust fronts: A case study. *Journal of Geophysical Research: Atmospheres*, 124, 2379–2396. <https://doi.org/10.1029/2018JD029832>

Received 14 OCT 2018

Accepted 6 FEB 2019

Accepted article online 8 FEB 2019

Published online 1 MAR 2019

## Convection Initiation Resulting From the Interaction Between a Quasi-Stationary Dryline and Intersecting Gust Fronts: A Case Study

Lanqiang Bai<sup>1,2</sup> , Zhiyong Meng<sup>1</sup> , Yipeng Huang<sup>3</sup> , Yunji Zhang<sup>4</sup> , Shuzhen Niu<sup>5</sup>, and Tao Su<sup>6</sup>

<sup>1</sup>Laboratory for Climate and Ocean-Atmosphere Studies, Department of Atmospheric and Oceanic Sciences, School of Physics, Peking University, Beijing, China, <sup>2</sup>Center for Monsoon and Environment Research, School of Atmospheric Sciences, and Guangdong Province Key Laboratory for Climate Change and Natural Disaster Studies, Sun Yat-Sen University, Guangzhou, China, <sup>3</sup>Laboratory of Straits Meteorology, Xiamen Meteorological Bureau, Xiamen, China, <sup>4</sup>Department of Meteorology and Atmospheric Science, and Center for Advanced Data Assimilation and Predictability Techniques, The Pennsylvania State University, University Park, PA, USA, <sup>5</sup>Henan Meteorological Bureau, Zhengzhou, China, <sup>6</sup>Zhejiang Institute of Meteorological Sciences, Hangzhou, China

**Abstract** This study explores the convection initiation (CI) of a high-impact squall line that occurred in central eastern China on 3 June 2009 based on observations and numerical modeling. The CI occurred in a scenario in which a set of intersecting gust fronts, organized in a distinct scalloped pattern, propagated toward an area of enhanced moisture produced by a near-surface convergence line. This convergence line developed in a quasi-stationary dryline zone. The dryline primed the preconvective environment by deepening the moist layer prior to the arrival of the intersecting gust fronts. The onset of CI occurred approximately 30 min after these intersecting gust fronts passed through the CI location, which was on the dry side of the dryline. Although these gust fronts acted as a strong signal for CI potential, CI did not occur along the entire length of the scalloped pattern of the intersecting gust fronts. The exact locations of the initiated convective cells were at the vertices of the scalloped pattern. An idealized simulation using a cloud model was conducted, demonstrating that the vertex regions were characterized by more favorable dynamical conditions for CI compared to the nonvertex regions along the scalloped outflow boundary. The greater CI probability over the vertex region was attributed to the greater magnitudes and larger vertical and horizontal extents of updrafts.

## 1. Introduction

A convection initiation (CI) event represents the initial formation of a deep moist convective cell that is characterized by a sustained, buoyantly forced main updraft (Ziegler, 2014). It is a process in which a potentially unstable air parcel passes through its level of free convection (LFC) to initiate buoyant updraft growth with the release of instability. The ability to forecast when and where a new convective system will be initiated is important for disaster preparedness; therefore, CI has been extensively researched in recent decades (e.g., Campbell et al., 2014; Markowski et al., 2006; Peters & Hohenegger, 2017; Su & Zhai, 2017; Trier et al., 2015; Weckwerth & Parsons, 2006; Wilson & Roberts, 2006; Zhang et al., 2019; Ziegler & Rasmussen, 1998). However, predicting the precise location and timing of CI remains a challenge partly due to the lack of spatially and temporally dense observations, especially in the planetary boundary layer (PBL). Additionally, there is currently a limited understanding of how the interactions of physical processes at different scales contribute to locally enhanced moisture pooling and vertical lift. This study discusses the CI process of a high-impact squall line that occurred in central eastern China on 3 June 2009, in which the CI resulted from the interaction between a quasi-stationary dryline and several intersecting gust fronts manifested in a scalloped pattern.

Various convergent boundaries (or zones) in the PBL usually act as precursors to a potential CI by providing locally enhanced lift, especially in moist and unstable environments. These boundaries include drylines, gust fronts, horizontal convective rolls, cold/warm fronts, quasi-stationary fronts, sea breeze fronts, topographically forced boundaries, and bores, as has been shown in previous field campaigns, such as CINDE (Wilson et al., 1988), CaPE (Wilson & Megenhardt, 1997), IHOP\_2002 (Wakimoto & Murphey, 2010; Weckwerth et al., 2004; Wilson & Roberts, 2006), VORTEX (Blanchard, 2008), COPS (Wulfmeyer et al.,

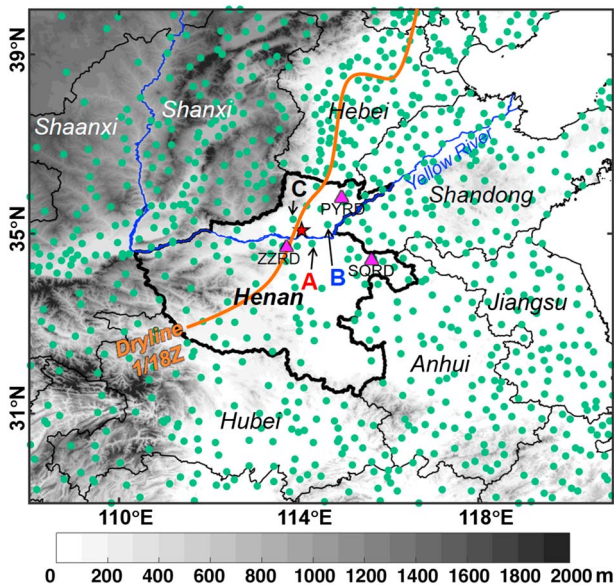


**Figure 1.** Terrain heights (shaded; m above mean sea level) and locations of in situ surface weather stations (green) around the target area in central eastern China. Henan Province is outlined in bold. Triangles denote the locations of the Zhengzhou (ZZRD), Puyang (PYRD), and Shangqiu (SQRD) radars. The red star represents the observed convection initiation location, and arrows point to the stations described in Figures 14 and 15. The orange curve denotes the identified dryline at 1800 UTC on 1 June 2009.

2008), UNSTABLE (Taylor et al., 2011), and PECAN (Geerts et al., 2017). Usually, a single PBL boundary seldom produces CI, likely due to the associated weak lift, while the interactions (e.g., merger, intersection, and collision) of multiple PBL boundaries often produce favorable conditions for the initiation or intensification of convection (e.g., Carbone et al., 1990; Droegemeier & Wilhelmson, 1985a, 1985b; Purdom, 1976, 1982; Weckwerth et al., 2008; Weiss & Bluestein, 2002; Wilson & Roberts, 2006; Wilson & Schreiber, 1986). The radar-based study by Wilson and Schreiber (1986) documented that 71% of boundary collision processes initiated new storms or intensified existing storms in the Denver, Colorado area. It usually takes approximately 15–30 min to initiate deep moist convection after boundary interactions (Intrieri et al., 1990; Wilson & Schreiber, 1986).

Drylines are often involved in PBL boundary interactions. Previous studies demonstrated that the interactions between drylines and other PBL boundaries, such as horizontal convective rolls (e.g., Atkins et al., 1998), gravity waves (e.g., McCarthy & Koch, 1982), and cold fronts (e.g., Koch & McCarthy, 1982; Qin & Chen, 2017; Wakimoto & Murphey, 2010; Weiss & Bluestein, 2002), were effective mechanisms for initiating deep moist convection. Dryline-associated CI in the United States has almost always been observed on the moist side of a dryline, because it is often too dry for CI to occur on the dry side (surface-level dew points often close to 0°C). The “triple points” formed by the interactions of drylines and baroclinic boundaries have been observed to be common locations for CI in the United States (e.g., Schumacher,

2015; Wakimoto et al., 2006; Weiss & Bluestein, 2002). Relative to the extensively discussed CI scenario of the cold front-dryline merger, as well as the intersecting “triple point” of a cold front and a dryline, the CI scenario that occurs when a series of gust fronts encounters a dryline zone has rarely been examined. This study presents a case in which CI occurred on the dry side of a dryline when gust fronts intruded into the dryline zone from the dry side.

In addition to recognizing the boundaries that can potentially initiate convection, it is also important to identify the factors that determine the precise location of CI, which is generally related to the spatial kinematic variability along a PBL boundary. Observational studies have shown that a scalloped (also called wave pattern) sea breeze front, which is often a recurring feature of coastal circulations, tends to configure local convergence and updraft maxima at the vertices of such a scalloped pattern (e.g., Kingsmill, 1995). Carbone et al. (1990) observed that the vertices of a wave pattern gust front were preferred regions for convection development. Strong horizontal wind shear across a PBL boundary is conducive to mesocyclone development, which can lead to a wave pattern boundary (e.g., Friedrich et al., 2005; Lee & Wilhelmson, 1997a, 1997b). The potential impacts of vertices (dynamical discontinuities) that form in intersecting gust fronts, rather than those that form due to shearing instability along a gust front, on CI have rarely been documented in the literature.

The present study aims to document a CI event that resulted from the interaction between a quasi-stationary dryline and a set of intersecting gust fronts that were organized in a scalloped pattern and to investigate what determined the exact location of CI along the entire length of the scalloped pattern. The data and methods are described in section 2. An overview of the selected CI event is presented in section 3. The evolutions of the PBL boundaries and CI mechanisms are discussed in section 4. Section 5 presents an idealized numerical experiment demonstrating the potential benefit of vertex structures on a scalloped outflow boundary for CI. Finally, a summary and brief discussion are presented in section 6.

## 2. Data and Methods

Observations from multiple platforms were used in this study to construct a three-dimensional structure of the CI process and its multiscale environment. Level II data collected at 6-min intervals from three S-band

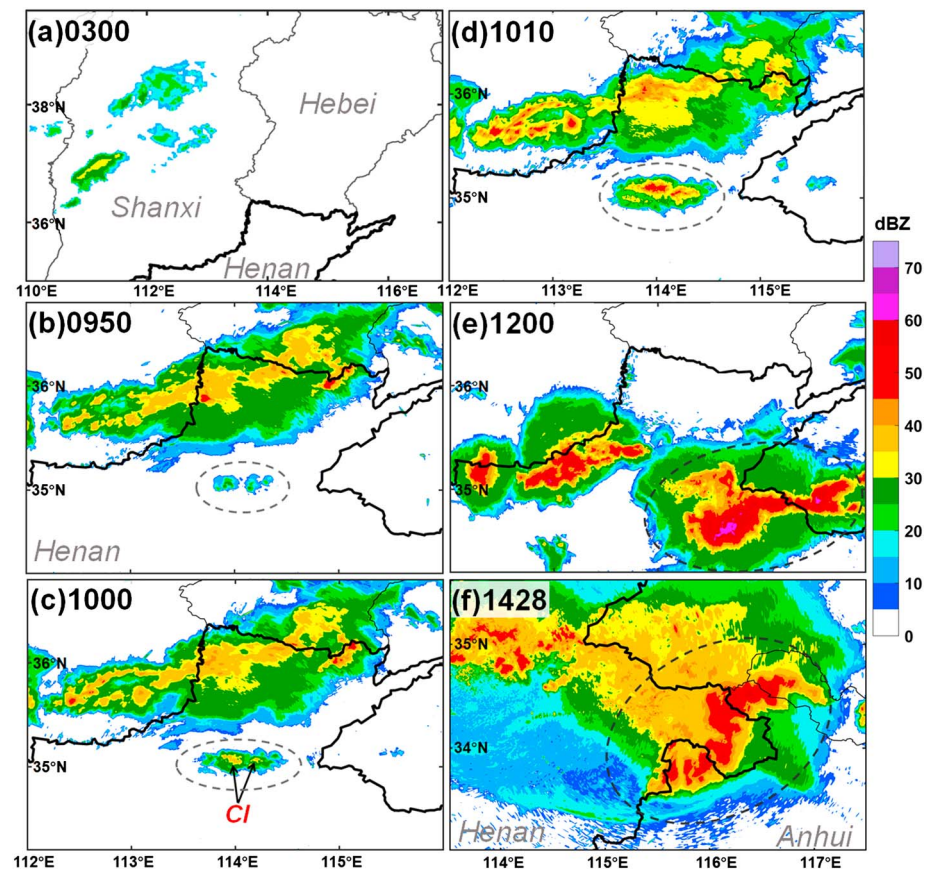


**Figure 2.** Composite radar reflectivity (shaded; dBZ) at different times (UTC) on 3 June 2009. The arrows in (c) indicate the initiated convective cells at the convection initiation time. The convective cells of interest are also indicated by dashed gray ellipses. Henan Province is outlined in bold.

Doppler radars located in Zhengzhou (ZZRD), Puyang (PYRD), and Shangqiu (SQRD) in Henan Province, China (Figure 1) were used to illustrate the detailed evolution of PBL boundaries and initiated storms. These radars are similar to WSR-88Ds in terms of both their hardware and software (Zhu & Zhu, 2004). Visible images from *Fengyun-2C* (*FY-2C*), a geosynchronous meteorological satellite operated by the National Satellite Meteorological Center of the China Meteorological Administration, were available every 30-min with a resolution of 1.25 km at nadir (Zhuge et al., 2011). Given the generally good representation of the synoptic atmospheric features and the 3-hr availability for the Global Forecast System (GFS) analysis (gridded on  $0.5^\circ \times 0.5^\circ$ ) in this case, we used the GFS analysis data mainly for synoptic-scale analysis. Other data used to analyze the CI environment included hourly surface observations from in situ surface weather stations (the stations around the study area are depicted in Figure 1) and operational radiosonde observations. During this event, surface observations recorded at 1-min intervals from the surface weather stations in Henan Province were also available. The recorded 1.5-m temperature and 1.5-m relative humidity data were instantaneous values, while the recorded 10-m surface wind values at each station represented the average values within 1 min.

In this study, CI was defined as occurring when the composite radar reflectivity in deep moist convection first reaches 35 dBZ (e.g., Kingsmill, 1995; Weckwerth, 2000). An observed gust front was identified based on low-level radar reflectivity and radial velocity fields when the leading edge of a moving “fine line” met the following conditions: (1) It clearly moved away and was completely disjointed (i.e., at least 10 km apart) from its parent thunderstorms; (2) it had a length of at least 10 km and lasted for at least 15 min (Wilson & Schreiber, 1986); and (3) it was accompanied by a sharp decrease in surface temperature after its passage. The position of a modeled gust front was objectively defined by tracing the movement of the relative

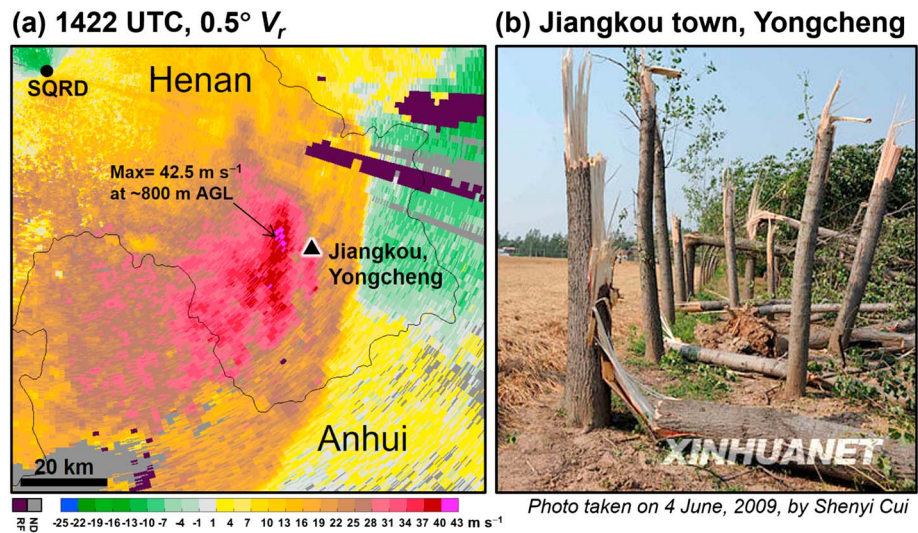


**Figure 3.** (a) Radial velocity ( $V_r$ ; m/s) at the  $0.5^\circ$  elevation angle from the Shangqiu (SQRD) radar (black dot) at 1422 UTC on 3 June 2009. The arrow points to the pixel that represents the maximum  $0.5^\circ V_r$  (42.5 m/s at  $\sim 800$  m above ground level). The triangle indicates the rough location of the (b) postevent photo that was taken on 4 June 2009 at Jiangkou town, Yongcheng City, by Shenyi Cui.

maximum magnitude of the horizontal velocity gradient tensor  $|\nabla_h \mathbf{V}_h|$ , where  $\mathbf{V}_h$  is the horizontal velocity vector (e.g., Stonitsch & Markowski, 2007) at the near-ground grid level.  $|\nabla_h \mathbf{V}_h|$  is calculated by

$$|\nabla_h \mathbf{V}_h| = \sqrt{\frac{1}{2} \sum_{i=1}^2 \sum_{j=1}^2 \left( \frac{\partial u_i}{\partial x_j} \right)^2}. \quad (1)$$

The leading edge of such a defined maximum zone was regarded as a gust front if it emanated from a storm and was accompanied by a sharp decrease in surface temperature after its passage. A boundary with a large horizontal moisture gradient, termed the dryline, typically has a dew point gradient magnitude of  $10 \text{ K (100 km)}^{-1}$  (Coffer et al., 2013) or a specific humidity gradient magnitude of at least  $3 \text{ g/kg (100 km)}^{-1}$  (Hoch & Markowski, 2005). In the present study, a dryline was defined when a boundary was accompanied by a surface dew point gradient of  $\geq 10 \text{ K (100 km)}^{-1}$  and it was not a result of thunderstorm outflows or cold fronts. The position of a dryline was determined by outlining the isopleth (dew point gradient magnitude) of  $5 \text{ K (100 km)}^{-1}$  on the moist side of the dryline zone, which was generally associated with the sharpest dew point gradient.

### 3. Review of the 3 June 2009 Case

The CI of interest occurred in close proximity to the Yellow River and on the plain in Henan Province, which was bordered to the west by a plateau in central eastern China (Figure 1). The onset of CI took place at 1000 UTC on 3 June 2009 (UTC = Beijing Time-8 hr; Figure 2). Two distinct convective cells (Figures 2b–2d) were initiated after the arrival of several intersecting gust fronts that emanated from the thunderstorms to the north (the echoes to the north of the ellipse in Figure 2b). After the convective cells (refer to the ellipses in Figure 2) were initiated, they merged and rapidly developed into an intense squall line characterized by a well-defined bow echo (e.g., Figure 2f).

This high-impact squall line produced strong downbursts and widespread wind damage ranging from eastern Henan Province to the neighboring regions of Shandong, Henan, Anhui, and Jiangsu provinces on the evening of 3 June 2009, causing 27 fatalities (Zhang et al., 2012). In fact, this region has the highest recorded rate of squall line incidents in China (He et al., 2017; Huang et al., 2017; Meng et al., 2013, 2018). The bow echo reached its peak intensity at  $\sim 1422$  UTC, with a maximum radial velocity of 42.5 m/s at the  $0.5^\circ$  elevation angle ( $\sim 800$  m above ground level) over Yongcheng City (Figure 3a). The observed maximum

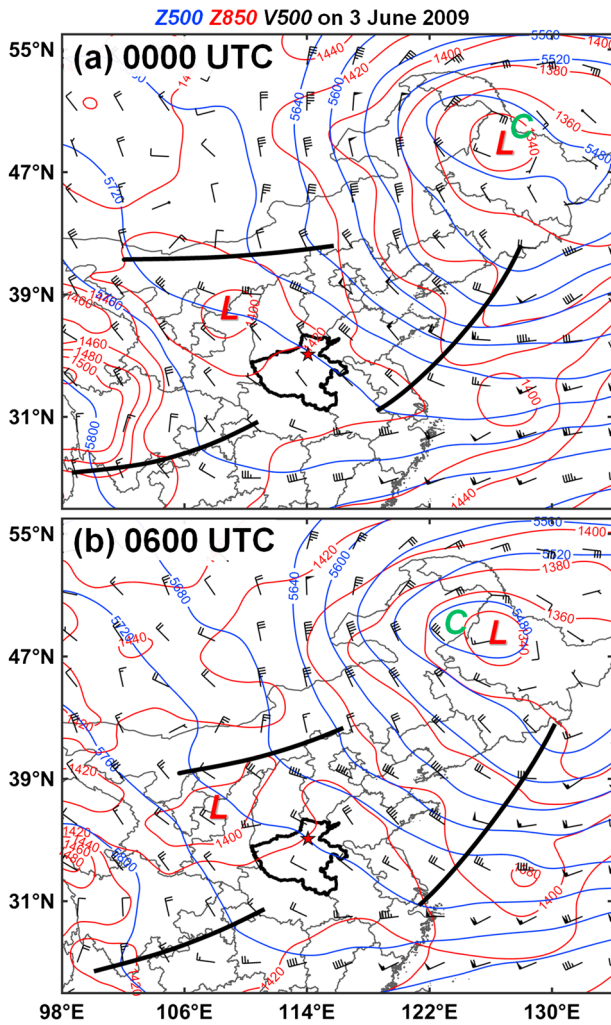


**Figure 4.** Global Forecast System analyses of 500-hPa (blue) and 850-hPa (red) geopotential heights (gpm) and 500-hPa winds at (a) 0000 and (b) 0600 UTC on 3 June 2009. The thick black curves denote the individual bases within the larger-scale trough at 500 hPa. Capital letters “C” and “L” denote the 500-hPa cold centers and 850-hPa low-pressure centers, respectively. The convection initiation location is denoted by a red star, and Henan Province is outlined in bold. The half barb, full barb, and pennant represent 2, 4, and 20 m/s, respectively.

0000 UTC (10 hr before CI). The large-scale environment in Henan Province was examined based on this sounding, while the near-storm environment was analyzed by assuming a well-mixed boundary layer due to daytime heating (e.g., Crook, 1996). It is important to note that the approach of modifying the PBL data was applied for lack of better sounding observations.

According to the original sounding, large surface-based convective inhibition (SBCIN) exceeding 1,200 J/kg and fairly small surface-based convective available potential energy (SBCAPE; only 85 J/kg) were observed because of the strong temperature inversion below 925 hPa (Figure 7). To obtain a more representative pre-convective environment, the sounding was modified by assuming a well-mixed boundary layer using the observed surface temperature (35 °C) and dew point (13 °C) at 0900 UTC (1 hr before CI) at a station close to the CI location (station A marked in Figure 1). The modified SBCAPE reached 1,695 J/kg (refer to the dashed red curve in Figure 7), with an SBCIN value of 153 J/kg. This SBCIN was still relatively large. The computed convective temperature was approximately 39 °C, which was 2 °C higher than the maximum surface temperature recorded throughout all of Henan Province on 3 June 2009. It is worth noting that this

instantaneous surface wind speed was 29.5 m/s, as recorded by an in situ surface weather station in Yongcheng City at 1420 UTC (Niu et al., 2012). Numerous trees in the Jiangkou town of Yongcheng were snapped (e.g., Figure 3b). The majority of damaged trees were aspens (softwood). Based on these damaged aspens, the wind speed estimate for the corresponding degree of damage was assigned the expected value of 46.5 m/s (Wind Science and Engineering Center, 2006), rated EF1 (38–50 m/s) on the enhanced Fujita scale. This estimate reasonably suggests that the peak surface wind gust was at least 46.5 m/s, which is close to the maximum 0.5° radial velocity of 42.5 m/s measured near this location. This result supports the possibility of using the 0.5° radar radial velocity to make short-term warning of surface damaging winds, at least in this case.

The synoptic-scale environment prior to the CI event was characterized by a short-wave trough (~1,000 km; the upper-left trough in Figure 4) that was embedded in a quasi-stationary large-scale cold vortex (low-pressure system with an upper-level cold core) in Northeast China with a horizontal radius of ~1,000 km. The 3 June squall line was actually the first of three severe mesoscale convective systems that occurred in central eastern China in this cold vortex environment during the first half of June 2009 (e.g., Su & Zhai, 2017). In front of this short-wave trough, there was a low-pressure center at 850 hPa (Figure 4) and at the surface (Figure 5a). The surface low-pressure zone extended from Shaanxi Province through Henan Province all the way to Jiangsu Province (province locations are given in Figure 1). As the short-wave trough moved downstream (Figure 4), a series of storms continuously formed over Shanxi Province from 0130 UTC on 3 June 2009 (e.g., Figures 2a and 6a). As these thunderstorms moved to the east southeast, the convection of interest was initiated to the south of these thunderstorms in Henan Province (Figure 2).

Sounding analysis, as will be shown below, indicated that the convection was more likely to have been initiated dynamically than by daytime heating. It was difficult to find a sounding that was representative of a near-storm environment, especially given the presence of mesoscale variability in the PBL (Markowski et al., 1998). If the proximity sounding is collected relatively far, either spatially or temporally, from a severe storm, it tends to be more representative of the larger-scale environment than of the storm environment (Potvin et al., 2010). In the present case, the sounding spatially and temporally closest to the CI of interest was obtained from the operational radiosonde that was launched at Zhengzhou (~50 km to the southwest of the CI location; refer to the ZZRZD in Figure 1) at

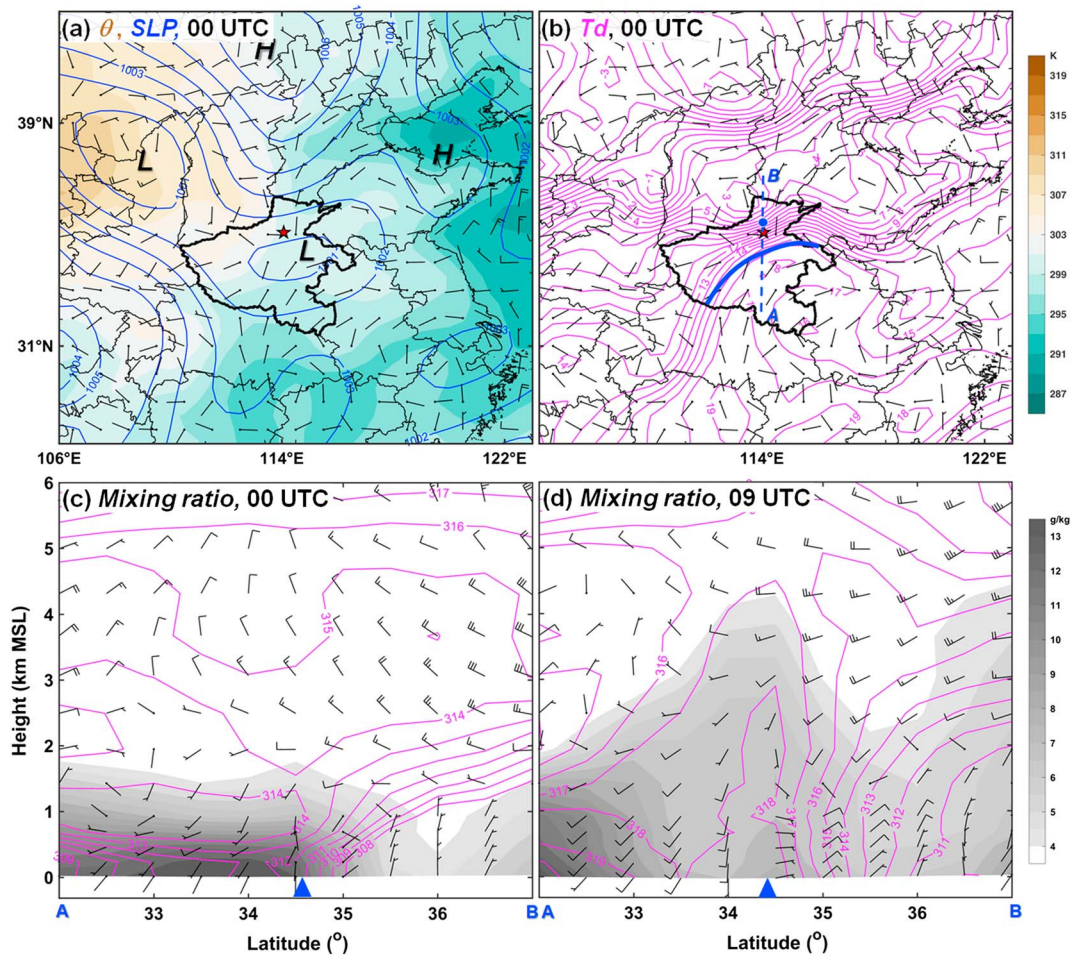


**Figure 5.** Global Forecast System analyses valid at (a–c) 0000 and (d) 0900 UTC on 3 June 2009. In (a), sea level pressure (contoured every 1 hPa in blue) and surface potential temperature (shaded; K) are presented. Capital letters “H” and “L” denote the centers of the high- and low-pressure zones, respectively. Surface winds are also shown in (a) and (b). In (b), surface dew points are contoured every 1°C in magenta, and the analyzed dryline located in Henan Province is denoted by the solid blue curve. The blue dot is where the sounding in Figure 17a was located. The CI location is denoted by a red star, and Henan Province is outlined in bold. (c and d) Vertical sections of water vapor mixing ratio (shaded; g/kg), horizontal winds, and equivalent potential temperature (contours; K) along the dashed blue line “AB” in (b). The blue triangle denotes the approximate location of the dryline. The half barb, full barb, and pennant represent 2, 4, and 20 m/s, respectively.

sounding was taken 10 hr prior to the onset of CI, and the obtained convective temperature may have been lowered due to potential synoptic preconditioning. Although the convective temperature could have been lowered, it still likely represents the need for extra mesoscale lifting to initiate convection. Besides, the high value of convective inhibition was conducive to the accumulation of thermodynamic energy in the boundary layer and thus could be indicative of subsequent high convective severity.

## 4. PBL Boundaries and CI Mechanisms

### 4.1. Role of the Quasi-Stationary Dryline

Two days before the onset of CI, a distinct dryline formed in Henan and Hebei provinces that was generally parallel to the western mountain range (Figure 1). After its formation, the dryline moved to the southeast, with its southern part remaining quasi-stationary in Henan Province from 0200 UTC on 2 June 2009 (Figure 8). On the dry side of the dryline, the surface dew points were approximately 10 °C, which was approximately 10 °C lower than those on the moist side, while the overall surface temperature was 1–2 °C greater than that on the moist side (Figure 8). The dew point gradients normal to the dryline were not attributed to a cold front or thunderstorm outflows because it was cloudless to the north of Henan Province before 0000 UTC on 3 June 2009. Apparent horizontal wind shear was also observed across the dryline.

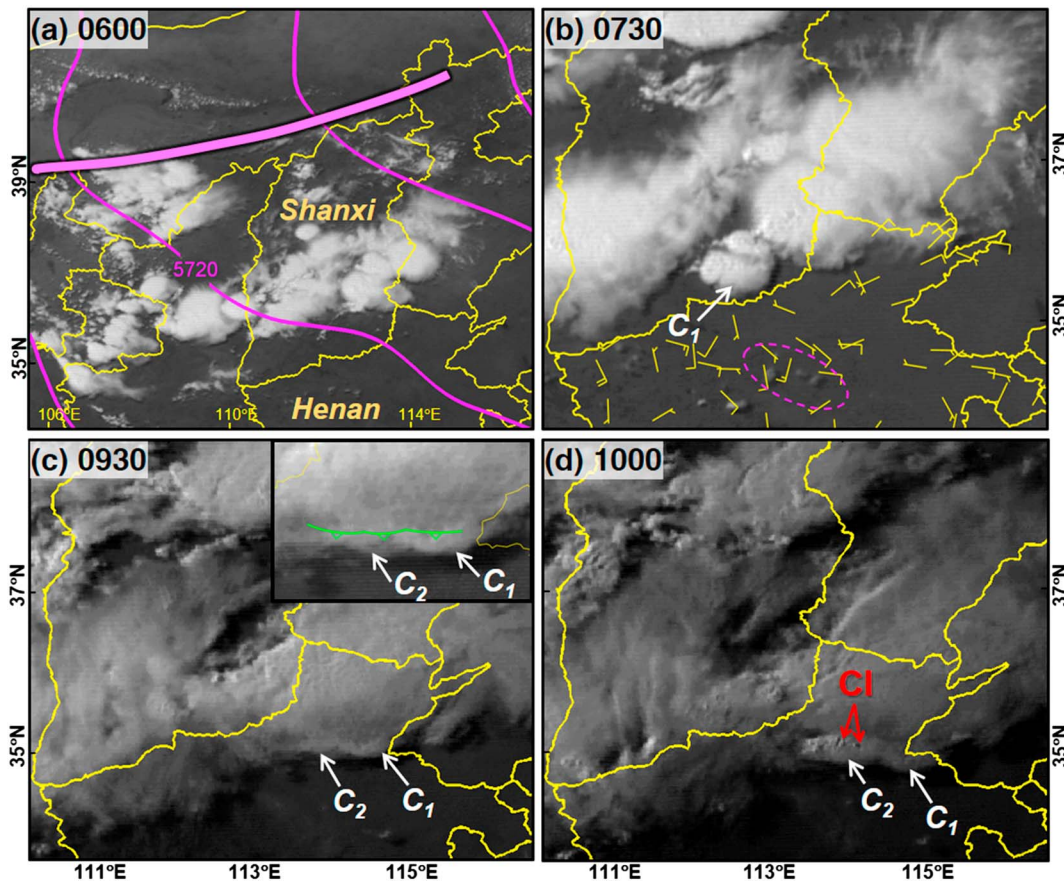


**Figure 6.** FY-2C satellite images (visible channel) at different times (UTC) on 3 June 2009. The thick and thin magenta curves in (a) represent the 500-hPa short-wave trough and the 500-hPa geopotential height (contoured every 40 gpm), respectively. The white arrows labeled  $C_1$  and  $C_2$  in (b)–(d) point to the cloud lines described in the text. The cloud lines were identified according to the cloud evolution at different times. They were observed to newly develop in proximity to the clear edge of the northern clouds. The dashed magenta ellipse in (b) outlines the shallow cumulus clouds described in the text. The 10-m winds at 0730 UTC in Henan Province are also shown in (b). The half barb, full barb, and pennant represent 2, 4, and 20 m/s, respectively. Gust fronts #1–3 are outlined in green in the enlarged convection initiation region in (c), according to the leading edge of the  $0.5^\circ$  radar fine lines that are superposed onto the satellite image. The red arrows in (d) indicate the locations of the two initiated convective cells (refer to Figure 2c).

GFS analyses showed that this dryline formed at the intersection of a low-level moist layer from the south and mountainous terrains to the west, with westerlies near the surface of the mountains (Figure 9a). The Zhengzhou sounding at 1200 UTC on 1 June 2009 revealed a dry elevated mixed layer above a capping inversion (Figure 7b), which was similar to the dryline environment that are often observed in the United States (e.g., Weiss & Bluestein, 2002; Ziegler et al., 1997). The western mountainous terrain may have partly contributed to the dryline formation by causing turbulent mixing with daytime heating around the mountain edges, and the gradients of near-surface moisture may have been additionally strengthened by the downward transport of horizontal momentum in the dry air over these mountains (Figure 9).

The quasi-stationary dryline primed the preconvective environment by deepening the moist layer around the CI location due to the near-surface convergence. With the enhancement of the northerly component on the dry side, the moisture content greater than  $4 \text{ g/kg}$  extended from  $\sim 1.8$  to  $\sim 4 \text{ km}$  above mean sea level over the dryline zone from 0000 to 0900 UTC due to the forced ascent by low-level convergence (Figures 5c and 5d). The deepening moist layer could have reduced the dilution of subsequent ascending air parcels (Lock & Houston, 2014), creating a favorable environment for the initiation of deep moist convection.

Surface station observations revealed more detailed variability along the southwest–northeast dryline zone compared to the results of GFS analysis. The dryline evolved from a nearly straight line to a wave pattern with a moist bump developing northward to the CI location. At 0000 UTC on 3 June 2009, central Henan Province was characterized by a surface low (Figure 8b). With the intensification and southeastward

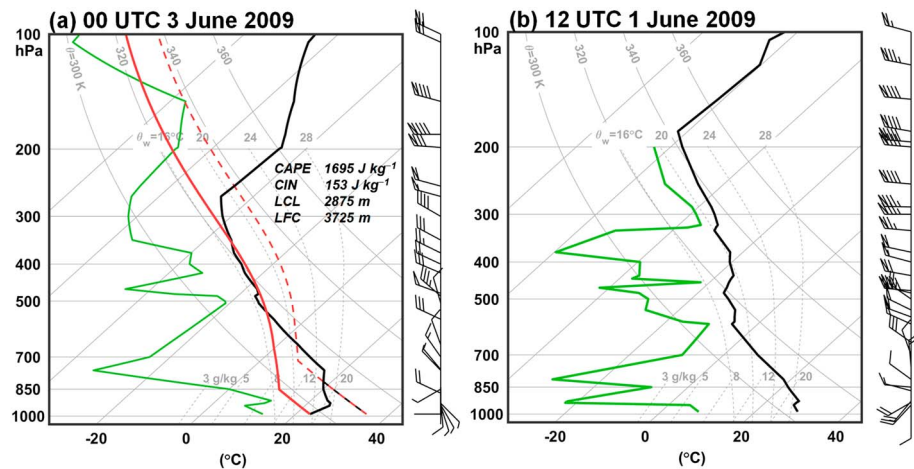


**Figure 7.** Skew  $T$ - $\log p$  diagram showing the radiosonde observation at Zhengzhou (refer to ZZRZ in Figure 1) at (a) 0000 UTC 3 June 2009 and (b) 1200 UTC 1 June 2009. The ambient temperature and dew point are represented by the solid black and green lines, respectively. In (a), the parcel that ascends undiluted from the surface is indicated by a solid red line. To obtain a more representative preconvective environment, the sounding was modified by assuming a well-mixed boundary layer using the observed surface temperature (35 °C) and dew points (13 °C) at 0900 UTC (1 hr before convection initiation) at station A (shown in Figure 1). The modified ambient temperature (without virtual temperature correction) is plotted by the dotted black line, and the new parcel ascent curve is indicated by the dashed red line. The surface-based (with virtual temperature correction) CAPE, CIN, LCL, and LFC values were obtained using the modified sounding. The half barb, full barb, and pennant represent 2, 4, and 20 m/s, respectively.

extension of this low-pressure disturbance, a distinct surface convergence line formed in a southeast-northwest orientation from 0300 UTC, producing a local maxima of near-surface moisture and causing the dryline to retreat to the dry side (e.g., Figures 8c and 8d). The dryline bulge close to the convergence line at 0700 UTC was a result of advection and intensification of the bulge feature at 0300 UTC (Figure 8d). The mesoscale bulges (toward the dryline moving direction) or low-pressure zones along a dryline are sometimes observed to be preferred locations for CI (e.g., Bluestein et al., 1988; Hane et al., 1997). In the present case, it was an “opposite” bulge (relative to the dryline motion) along the dryline. With increasing convergence along the convergence line (e.g., Figure 10), a northwest-southeast radar fine line was identified, corresponding to the convergence line (an example of a legible radar fine line at 0900 UTC is shown in Figure 11). This convergence line slowly moved toward the northeast in the reflectivity and radial velocity fields at the 0.5° to 2.4° elevation angles (~700–2,300 m above radar level) from approximately 0600 UTC (not shown). Corresponding to the northeastward movement of the convergence line, the local near-surface moisture maxima and also the opposite bulge of the dryline moved increasingly closer to the CI location. Small shallow cumulus clouds were also observed over this convergence line (e.g., Figure 6b). The closest distance between the determined dryline and the CI location was approximately 25 km 1 hr prior to the CI.

Even though the convergence line had moistened the mesoscale environment in the proximity of the CI location, the CI location was still relatively dry 1 hr before the onset of CI due to its being located on the dry side of the dryline zone (e.g., Figure 10). The moisture content around the CI location was ~9 g/kg, and the relative humidity was approximately 30%. Such a relatively dry preconvective environment likely represents the need for strong mesoscale forced lift to initiate deep moist convection.

#### 4.2. Role of Outflow Boundaries

Outflows from the northern thunderstorm cold pools (refer to dark blue regions in Figure 12) started to affect northern Henan Province at approximately 0800 UTC on 3 June. The outflows were inferred to promote the CI via the enhanced lift provided by a set of gust fronts intruding into the dryline zone.

The gust fronts that emanated from the northern thunderstorms were first identified slightly to the north of station B (location is given in Figure 1) at 0842 UTC. These gust fronts could be seen as a sequence of southward moving radar fine lines (labeled #1–5, as shown in Figure 13). These fine lines were identified only at

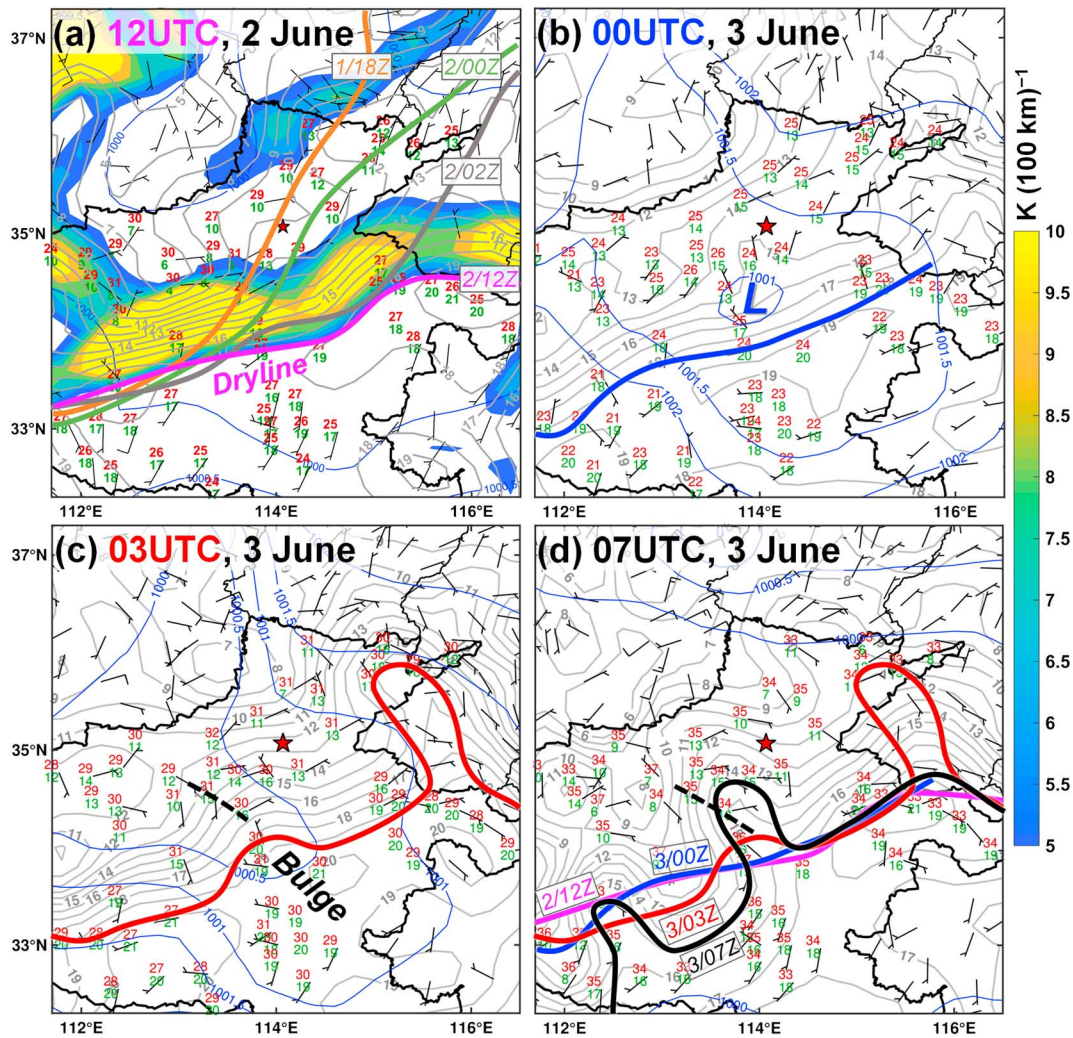


**Figure 8.** Surface analyses, including dew point (contoured every 1 °C in gray), sea level pressure (contoured every 0.5 hPa in blue), and 10-m winds at different times on 3 June 2009. The half barb, full barb, and pennant represent 2, 4, and 20 m/s, respectively. The shadings in (a) represent the horizontal gradients [ $\text{K} (100 \text{ km})^{-1}$ ] of dew point at 1200 UTC on 2 June 2009. The “L” in (b) represents the center of surface low. The convection initiation location is denoted by a red star. The dryline positions at different times (labeled by day/time) are plotted with heavy curves in different colors. The near-surface convergence line described in the text is marked by a dashed black line. The values of 1.5-m temperature (red) and dew point (green) at surface weather stations in Henan Province are labeled.

the 0.5° and 1.5° elevation angles. By examining the evolution of radial velocity fields (e.g., Figure 13b) and surface observations, these radar fine lines were determined to be gust fronts generated by the northern thunderstorms that were located at the northern end of Henan Province.

In the 7 min after ~0823 UTC, surface weather station C (location is given in Figure 1) recorded a surface temperature drop of 0.7 °C (Figure 14). According to the evolution of these radar fine lines, this sharp decrease in temperature was caused by gust front #1 (Figure 13) which passed through station C at that time. At 0900 UTC, the east-west oriented gust fronts #1 and #3 moved southward, while the southwest-northeast oriented gust front #2 moved toward the south-southeast. Radar and surface observations confirmed that gust fronts #1–3 arrived at station B at 0910 UTC, when the wind speed at station B started to dramatically increase (Figure 15a). Gust front #4 moved toward the south at a greater speed than gust fronts #1–3. This gust front passed through station C and caused a rapid temperature decrease of 1.0 °C within 9 min after ~0924 UTC (Figure 14).

The enhanced horizontal convergence around the CI location was revealed by examining the meteogram of the winds at surface weather stations. Stations A and B were closely located on the southern and northern sides of the CI location, respectively (Figure 15b). The meridional distance from station A to B was

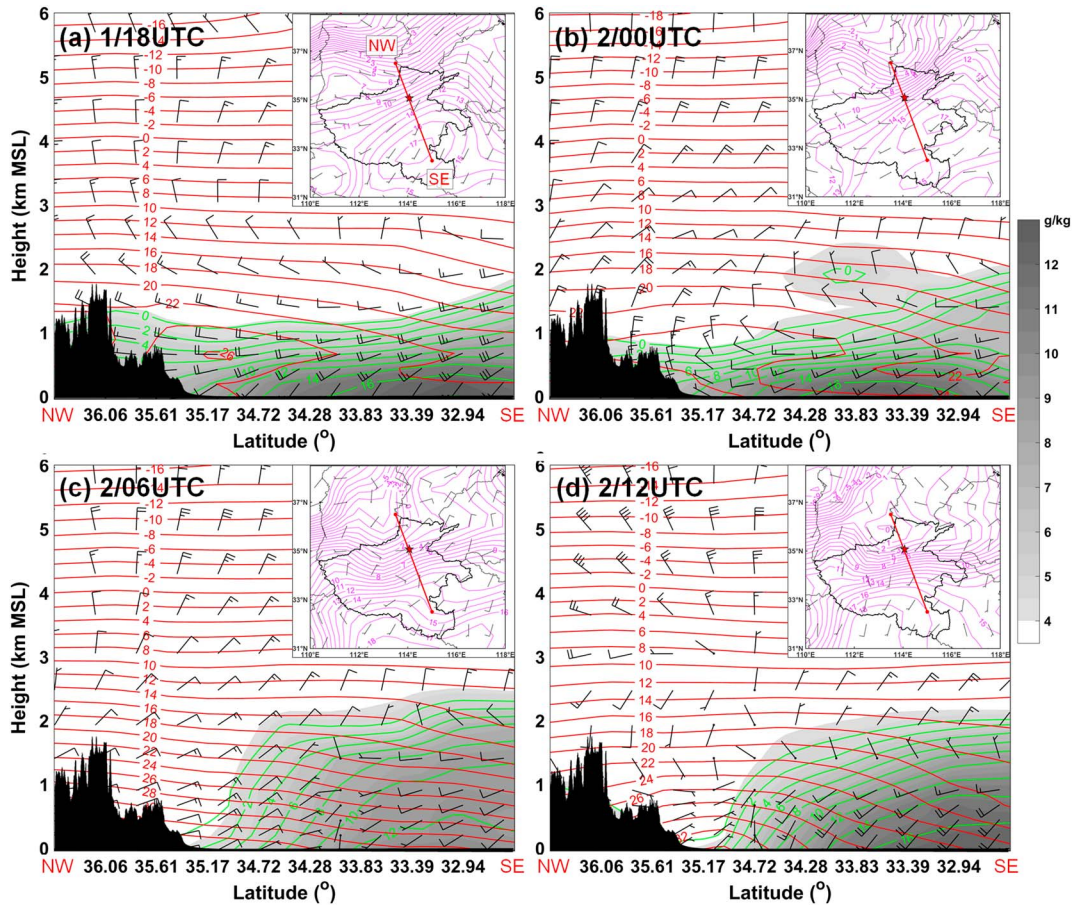


**Figure 9.** Vertical sections of water vapor mixing ratio (shaded in gray; g/kg), horizontal winds, dew points (green; °C) and temperature (contours in red; °C) along the red line shown in the inset of each panel. The data are from the Global Forecast System analysis valid at (a) 18 UTC on 1 June, and (b) 00, (c) 06, and (d) 12 UTC on 2 June 2009. The inset in each panel is the same as that in Figure 5b at the corresponding time. The terrain heights are shaded in black. The half barb, full barb, and pennant represent 2, 4, and 20 m/s, respectively.

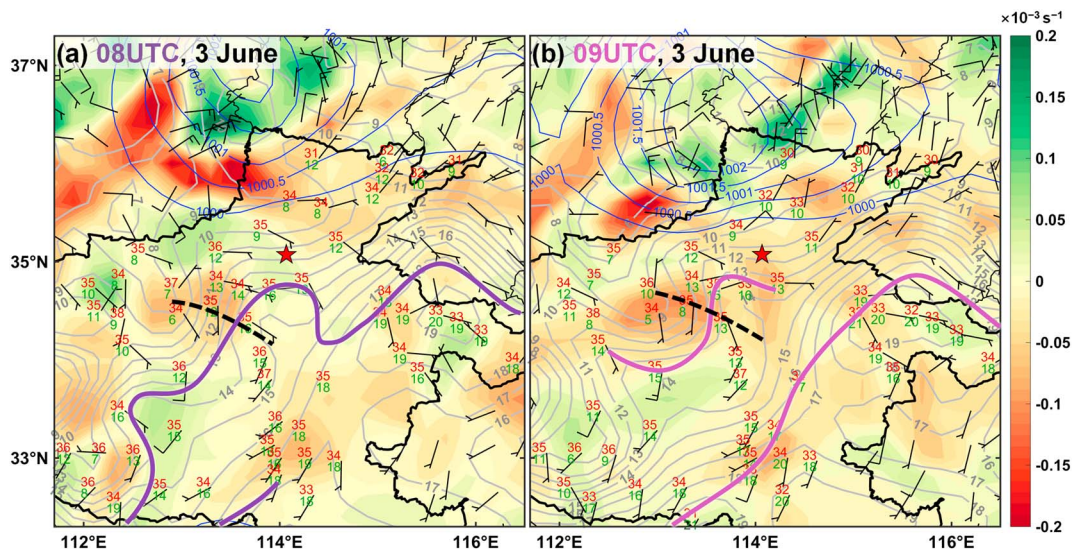


**Figure 10.** Same as Figure 8, except the shading represents horizontal divergence ( $\times 10^{-3} \text{ s}^{-1}$ ).

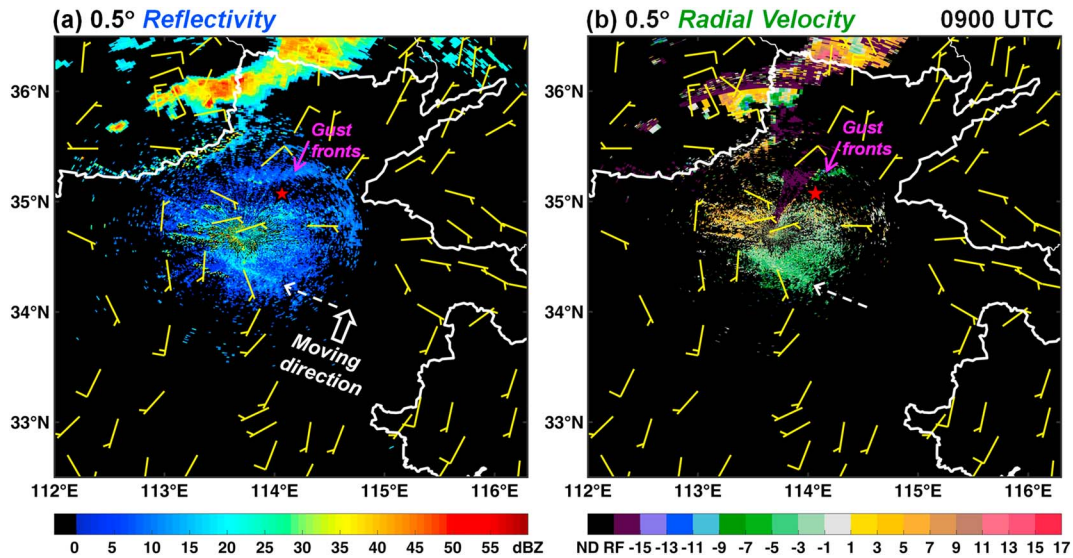


**Figure 11.** (a) Base reflectivity (shaded; dBZ) and (b) radial velocity (shaded; m/s) at the 0.5° elevation angle from the Zhengzhou radar at 0900 UTC on 3 June 2009. The 10-m winds at 0900 UTC from in situ surface weather stations are also plotted. The half barb, full barb, and pennant represent 2, 4, and 20 m/s, respectively. The convection initiation location is denoted by a red star. The dashed arrow points to the radar fine line associated with the near-surface convergence line. The large empty arrow in (a) indicates the rough direction of the movement of of this fine line.

46.6 km. At approximately 0800 UTC, the surface flow near the CI location was generally steadily from the east-southeast (Figure 12a). Approximately 27 min later, the surface flow to the north of the CI location generally started to turn toward the south (Figure 15a), which could have further enhanced the horizontal convergence by converging with the southerly wind (e.g., Figures 15a and 10). The CI position was located exactly within this enhanced convergence zone (refer to the wind directions at stations A and B shown in Figure 15a). After 0930 UTC, the winds at both stations were northerly, suggesting that the enhanced convergence zone associated with the enhanced northerly wind was already located to the south of station A. As a result, the location of CI was within or close to this enhanced convergence zone for approximately 1 hr (0827–0930 UTC; time period between the dashed lines in Figure 15a).

Gust front #2 was located nearby gust fronts #1 and #3; it finally intersected with them, resulting in a scalloped appearance with two distinct vertex structures, which were clearly observed after 0924 UTC (e.g., Figure 16 and V1 and V2 shown in Figure 13). The intersecting gust fronts #1–3 arrived at the CI location

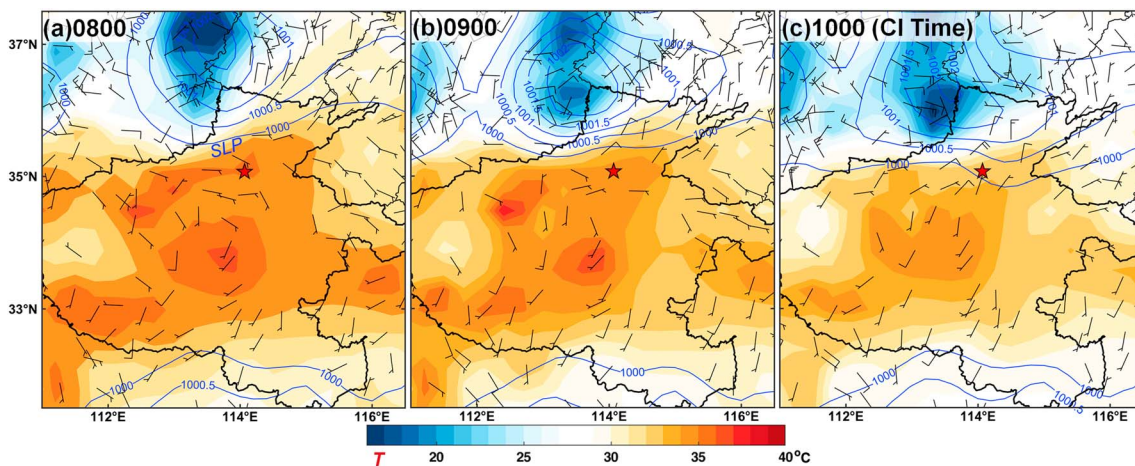


**Figure 12.** Surface analyses, including sea level pressure (contoured every 0.5 hPa in blue), 1.5-m temperature (shaded; °C), and 10-m winds from in situ surface weather stations at different times (UTC) on 3 June 2009. The half barb, full barb, and pennant represent 2, 4, and 20 m/s, respectively. The convection initiation location is denoted by a red star.

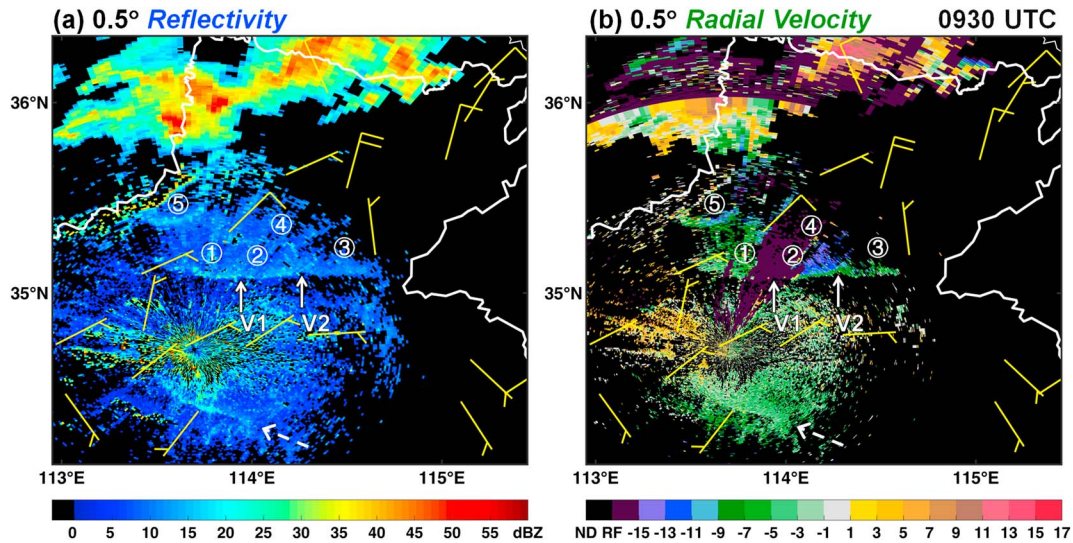


**Figure 13.** (a) Base reflectivity (shaded; dBZ) and (b) radial velocity (shaded; m/s) at the 0.5° elevation angle from the Zhengzhou radar at 0930 UTC on 3 June 2009. The solid arrows point to the vertices (“V1” and “V2”) of the scalloped pattern on gust fronts #1–3 (fine lines with numerical labels). The dashed arrow points to the same radar fine line as shown in Figure 10. The 1-min 10-m winds at 0930 UTC from in situ surface weather stations are also plotted. The half barb, full barb, and pennant represent 2, 4, and 20 m/s, respectively.

at 0930 UTC (Figure 15b) and maintained their east-west orientation (Figure 13). After this time, the surface winds at station A became northerly (Figure 15). Gust fronts #1–3 passed across the station A at approximate 1030 UTC (not shown).

The sensor onboard the *FY-2C* satellite scanned the area of interest at approximately 0934 UTC (note that the time shown in Figure 6 is the recorded time of the satellite data). At this time, the visible satellite imagery showed that an east-west cloud line ( $C_1$  and  $C_2$  in Figure 6) had developed over the CI region. The west part ( $C_2$ ) of this cloud line was first clearly identified at 0934 UTC and rapidly grew in the following 30 min (Figures 6c and 6d). This was the parent cloud of the convective cells that were initiated at 1000 UTC (refer to Figure 2c). The decaying cloud line  $C_1$  was not directly related to the CI because of the horizontal displacement of the CI region to cloud line  $C_1$  at the time of CI (Figure 6d).

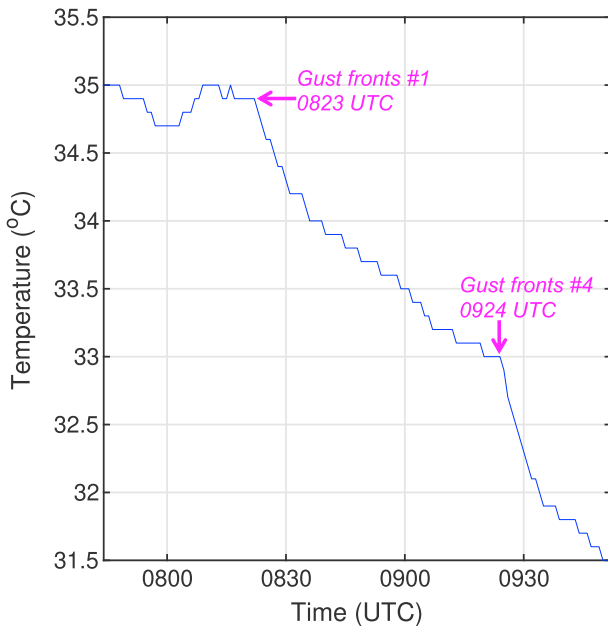


**Figure 14.** Meteogram of 1-min 1.5-m temperature (°C) at the in situ surface weather station C (location is shown in the inset of Figure 15b) on 3 June 2009.

Although the east-west cloud line  $C_2$  was located parallel to gust fronts #1–3, CI did not occur along the entire length of this cloud line. Two cells (~25 dBZ; “A” and “B” in Figure 16b) were first detected at 0948 UTC, which occurred exactly over the two vertices on the scalloped pattern of gust fronts #1–3. These two cells then experienced rapid growth within the next 12 min. The 35-dBZ echoes were observed to first occur at 8.8 km above mean sea level at 1000 UTC, representing the onset of CI. At this time, gust fronts #1–3 moved at least ~14 km to the south of the CI location (Figure 15b). Consequently, the convective cells of interest were initiated close to the vertices on the scalloped pattern of gust fronts #1–3 approximately 30 min after these gust fronts passed through the CI location. The 30-min period between the arrival of gust fronts #1–3 at the CI location and the onset of CI was consistent with the time required to grow precipitation size hydrometeors in deep convective circulations (Knight & Squires, 1982). Given the fact that gust front #4 was fast approaching to gust fronts #1–3, it is possible that gust front #4 might have promoted the CI process by increasingly intensifying the low-level convergence. However, gust front #4 was not the direct CI trigger. It arrived at the CI location at ~0954 UTC, while the convective cells had initiated at upper levels by the time of 0948 UTC (Figure 16b).

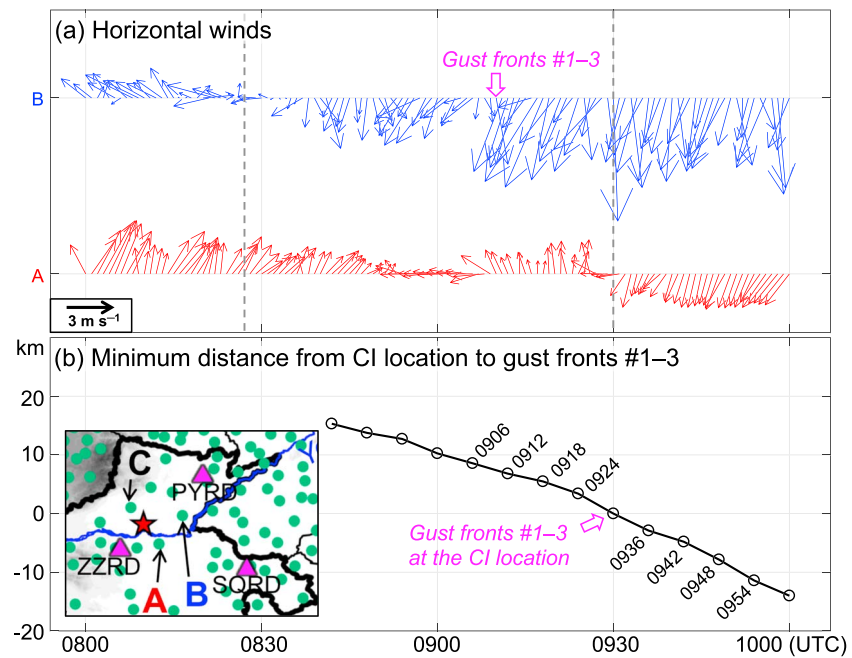


**Figure 15.** (a) Meteogram of the 1-min 10-m winds (the average within 1 min) at surface weather stations A (red) and B (blue) [locations are shown in the inset of (b)]. (b) Minimum meridional distance (black curve with circles) from the convection initiation location to the radar-identified gust fronts #1–3. The times of several radar observations are labeled for reference. The magenta arrow indicates the pass of gust fronts #1–3.

The above analyses revealed that CI occurred at the two vertices of gust fronts #1–3 when the gust fronts were moving into an environment with an increasingly deepening moist layer caused by a quasi-stationary dryline with a northward moist bump near the CI location.

### 5. Numerical Simulations of the Vertex Structures of Intersecting Gust Fronts

The vertices on scalloped boundaries are essentially the results of convergent boundary intersections and have been observed to be the preferred locations of enhanced low-level updrafts and thus the preferred locations for CI (Kingsmill, 1995) and convection development (Carbone et al., 1990). Wilson and Schreiber

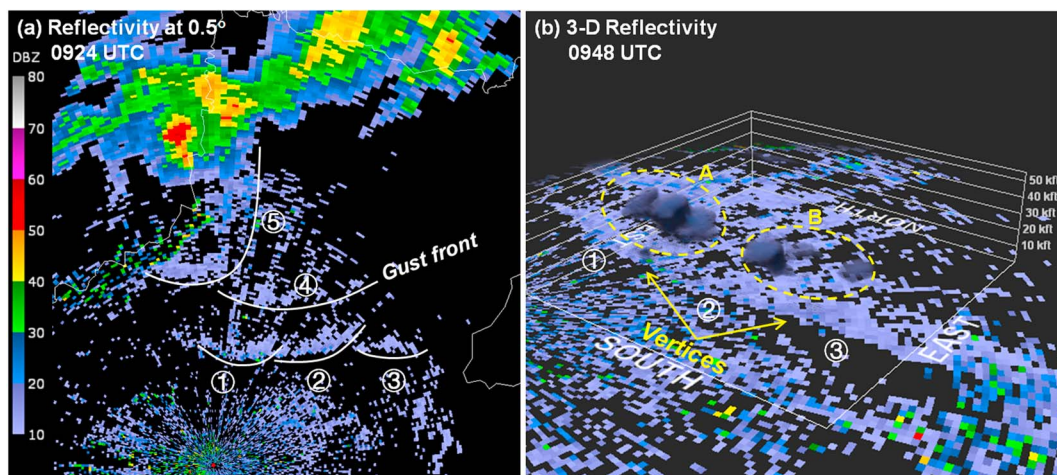


**Figure 16.** (a) Base reflectivity (shaded; dBZ) at the 0.5° elevation angle from the Zhengzhou radar at 0924 UTC on 3 June 2009. The radar fine lines indicating gust fronts are outlined by white curves with numerical labels. (b) Three-dimensional reflectivity (shaded; dBZ) from the Zhengzhou radar at 0948 UTC on 3 June 2009. The arrows point to the vertices of the scalloped pattern formed by gust fronts #1–3. The echoes denoted by the dashed ellipses indicate the convective cells of interest.

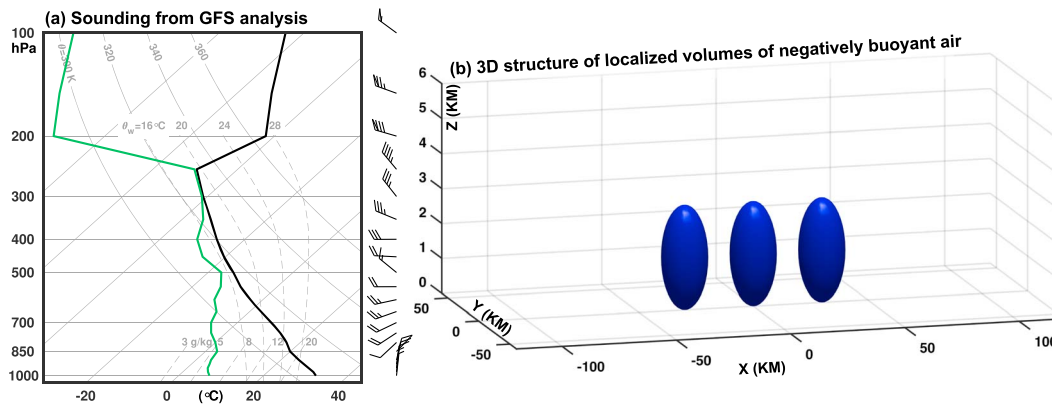


**Figure 17.** (a) Skew  $T$ -log  $p$  diagram showing the sounding obtained from the Global Forecast System analysis at the blue dot in Figure 5b at 0900 UTC on 3 June 2009. The ambient temperature (dew point) is represented by the black (green) curve. The half barb, full barb, and pennant represent 2, 4, and 20 m/s, respectively. (b) Schematic of three-dimensional structures of the localized volumes of negatively buoyant air (blue) in the initial condition of the idealized simulation. Axes indicate model coordinates (km).

(1986) documented that 64% of their convergent boundary intersection cases produced new storms and were conducive to storm intensification. Harrison et al. (2009) showed that 17% of their intersecting cases, in which two outflow boundaries produced intersection angles of  $100^{\circ}$ – $180^{\circ}$ , produced CI. In the present case, the angles at both the intersection points were close to  $180^{\circ}$ , and CI was observed to occur at both of these intersection points.

To explain why the vertex regions of boundaries are favorable for CI, Kingsmill (1995) provided convincing evidence that enhanced convergence and updraft motions existed at the vertices of a scalloped pattern of a sea breeze front by analyzing dual-Doppler radar-derived winds. Three-dimensional numerical simulations using idealized wind shear profiles obtained by Droegemeier and Wilhelmson (1985a, 1985b) have also supported the fact that the vertex regions of intersecting thunderstorm outflow boundaries promote cloud development. However, the difference between the vertical dynamical structure immediately across a vertex region compared to that across a nonvertex region on an outflow boundary has rarely been discussed. To examine the potential impact of such a difference on CI, especially by fine-resolution modeling, a three-dimensional numerical simulation was conducted to replicate the scalloped pattern of intersecting gust fronts under the environmental conditions of the present case. In real simulations, small-scale forecasting errors may grow very rapidly in moist convective process (Zhang et al., 2003), which may lead to large uncertainty in simulated small-scale processes (e.g., individual storm cells and their associated cold pools). Given

that an idealized simulation has the advantages in testing the validity of hypotheses in a “clean room” environment (e.g., Fovell et al., 2006), the simulations were designed in an idealized framework.

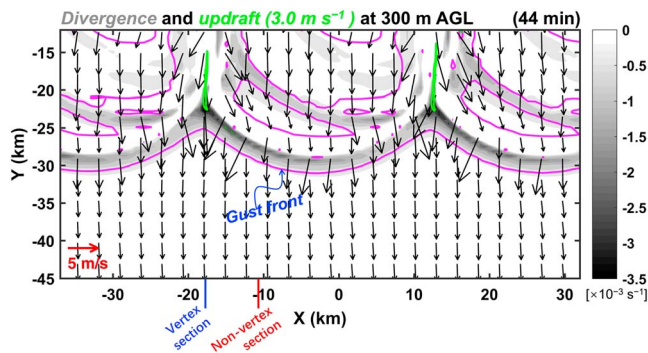


**Figure 18.** Horizontal divergence (shaded;  $\times 10^{-3} \text{ s}^{-1}$ ), updrafts ( $3.0 \text{ m s}^{-1}$  in green), and winds (vectors) at 300 m above ground level after 44 min of the model integration. The blue and red lines at the bottom indicate the locations of the vertical sections shown in Figure 20. The magenta contours represent the horizontal velocity gradient tensor with the magnitude of  $0.6 \times 10^{-3} \text{ s}^{-1}$ .

The idealized simulation was conducted using Cloud Model version 1 (CM1), release 18 (Bryan & Fritsch, 2002), which is a fully compressible and nonhydrostatic model. CM1 was configured in three dimensions ( $240 \times 240 \times 16 \text{ km}^3$ ) with rigid, free-slip top and bottom boundaries and periodic lateral boundaries. The horizontal and vertical grid spacings were 200 and 100 m, respectively. The simulation time was 60 min with a model time step of 0.5 s. The fifth-order advection scheme, which has implicit diffusion, was used, and no additional artificial diffusion was included. There were no surface fluxes, radiative transfer, or Coriolis force.

To idealize the interactions of multiple gust fronts in an environment as in the present case, the simulation was initialized with homogeneous environmental conditions using the sounding (Figure 17a) from the GFS analysis, which was obtained at 0900 UTC on 3 June 2009. This sounding was obtained at a location slightly to the north of the observed CI location

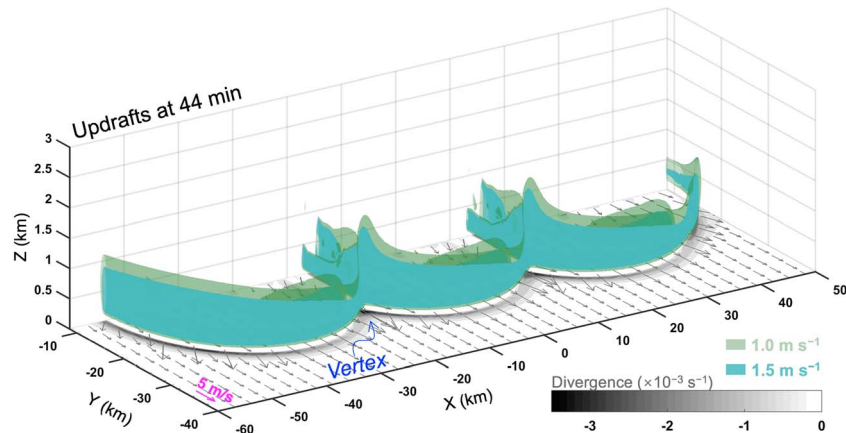


**Figure 19.** Three-dimensional updrafts (1.0 m/s in green and 1.5 m/s in cyan) and horizontal divergence (shaded in gray;  $\times 10^{-3} \text{ s}^{-1}$ ) with winds (vectors) at 300 m above ground level after 44 min of the model integration. The vector length scale is shown in magenta.

(refer to the blue dot in Figure 5b) in a similar environment as that of the observed gust fronts. Three localized volumes of negatively buoyant air were placed in the domain center and spaced 30 km apart along the  $x$  axis (Figure 17b). They were centered at a height of 1.5 km. Each volume had a horizontal radius of 10 km and a vertical radius of 1.5 km, with a minimum potential temperature perturbation of  $-6$  K. The potential temperature perturbation was minimized at the center and increased to 0 K following a cosine function over a horizontal (vertical) radius of 10 km (1.5 km).

This idealized simulation successfully produced a scalloped pattern of intersecting gust fronts that were organized in a similar manner to the observed scenario (e.g., Figure 18). Three intersecting gust fronts (indicated by narrow arc convergence zones) resulted in the appearance of maximum horizontal convergence and updrafts at the vertex regions along the scalloped boundary (Figures 18 and 19), which were consistent with the observational results obtained from the sea breeze front case in Kingsmill (1995). The vertex region was characterized by a broader zone of strong horizontal convergence compared to the nonvertex region.

The vertical section of updrafts across a vertex region (blue line below the  $x$  axis in Figure 18) was compared to that across nonvertex regions (red line below the  $x$  axis in Figure 18) along an outflow boundary. Under the environmental conditions characterized by the GFS sounding at 0900 UTC, the updraft over the vertex

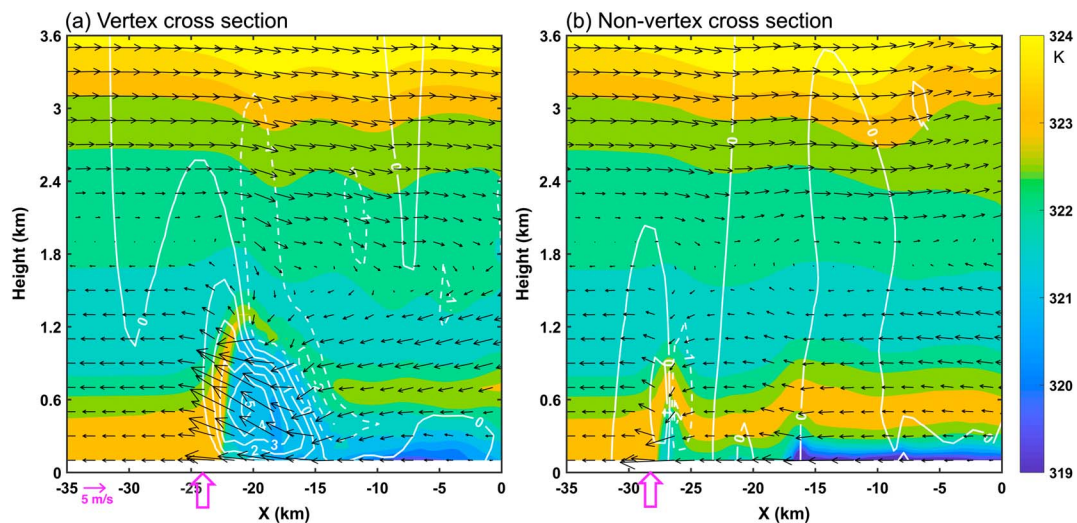


**Figure 20.** Vertical sections of vertical motions (contoured every 1 m/s in white), equivalent potential temperatures (shaded; K), and  $v$ - $w$  wind components (black vectors) across the (a) vertex and (b) nonvertex regions (refer to the blue and red lines shown below the  $x$  axis in Figure 18) on a scalloped outflow boundary after 44 min of the model integration. The magenta open arrows at the bottom indicate the approximate locations of the southernmost gust fronts as shown in Figure 18.

region was found to be distinctly larger than that over nonvertex regions (Figure 20). The magnitude of the maximum updraft over the vertex region was more than twice as large as that over the nonvertex region. Updrafts greater than 0 m/s also extended higher (to approximately 2.5 km above ground level) in the vertex region, which would strongly support the ability of low-level air masses to penetrate their LFC and consequently achieve a sustained, buoyantly forced main updraft. In addition to having a higher extent of updraft, the vertex region was also characterized by a broader horizontal range of updraft than other regions, which suggests that the air parcels in front of a vertex structure on a scalloped outflow boundary are subject to longer periods of updraft support (Figure 20).

## 6. Summary and Discussion

This study investigated the CI mechanism of a high-impact squall line that occurred in central eastern China on 3 June 2009. The initiation of the squall line occurred on the dry side of a quasi-stationary dryline with the intrusion of a set of intersecting gust fronts from the dry side. The dryline produced a favorable mesoscale environment for CI by deepening the moist layer around the CI region. The bulging of the dryline put the dry-wet air mass boundary close to the CI location, which made the thermodynamic environment more favorable for CI. A surface low-pressure disturbance along the dryline produced a northwest-southeast convergence line on the dry side of the dryline. This convergence line generated a local near-surface moisture maxima and caused the dryline to retreat to the dry side. Both the convergence line and the dryline moist bump gradually moved to the northeast, causing the local moisture maxima to move increasingly closer to the CI location. Although the local moisture maxima were near the location of CI, the moisture content was still not high (only  $\sim 9$  g/kg) at the CI location, and the relative humidity was less than 30% at the ground level before the onset of CI. Such a relatively dry surface-level environment suggests the need for a strong forced lift to achieve CI despite the occurrence of a deepened moist layer.

The CI was initiated by a set of intersecting gust fronts when they approached the deepening moist layer produced by the quasi-stationary dryline. The foremost three intersecting gust fronts were manifested in an east-west scalloped (or wave-like) pattern. Two convective cells were separately initiated close to the two vertices of the scalloped pattern. These two initiated cells then merged with each other and rapidly grew upscale to form a squall line.

An idealized simulation was used to reveal the potential benefit of vertex structures on scalloped intersecting gust fronts for CI, especially by assessing the differences between the three-dimensional dynamical structures at the vertex regions and those of nonvertex regions along the scalloped pattern. The simulated results were consistent with those of previous observational studies on scalloped PBL boundaries. The vertex region was characterized by more favorable dynamical conditions for CI compared with the nonvertex region, including greater magnitudes of maximum updrafts and larger extents of vertical and horizontal updrafts. A higher updraft depth tends to increase the probability that an air mass will penetrate its LFC; the larger horizontal extent of an updraft can lengthen its lifting time, which consequently further increases the probability of CI.

The results of this study could provide a helpful reference for CI nowcast. When a set of intersecting gust fronts move toward a dryline, CI may occur before the gust fronts intrude into the moist air masses (i.e., CI occurs on the dry side of the dryline). The exact CI (if any) locations are most likely located at the vertex regions on the scalloped pattern of these intersecting gust fronts.

Although the idealized modeling framework replicated the intersecting gust fronts, the simplified configuration does not completely represent the real-world CI scenario. A real numerical modeling is required to deeply investigate the interactions of multiscale physical processes that contributed to locally enhanced moisture pooling and vertical lift. To adequately forecast or simulate the exact location and timing of such a complicated CI event, a real numerical model needs to sufficiently accurately capture all of the aforementioned features (e.g., short-wave trough, surface low, preexisting thunderstorms, quasi-stationary dryline, surface convergence line, intersecting gust fronts), especially the PBL convergent boundaries and their interactions and structures (e.g., Wilson & Roberts, 2003). Although state-of-the-art mesoscale NWP models can generally capture synoptic-scale features well, they still have difficulties in accurately predicting the details of mesoscale features. In particular, small-scale errors associated with moist convection can rapidly grow in scale and amplitude (Zhang et al., 2003), which can influence cold pools (or gust fronts) and further affect

later CI and storm organization (Zhang et al., 2016). Consequently, such multiple-forcing-associated CI events may have a relatively low predictability (with correct CI mechanisms), which remains to be addressed in future studies.

#### Acknowledgments

We thank Matthew Parker from North Carolina State University and Russ Schumacher from Colorado State University for their valuable comments on the dryline. This work was supported by the Natural Science Foundation of China (grant 41425018) and the Ministry of Science and Technology of China (grant 2013CB430104). Surface, radiosonde, and radar data were provided by the National Meteorological Information Center of China Meteorological Administration (<http://www.cma.gov.cn/2011qxw/2011qsjgx/>). The GFS analysis data were downloaded from this website (<https://www.ncdc.noaa.gov/data-access/model-data/model-datasets/global-forecast-system-gfs>). The satellite observations were downloaded from this website (<http://satellite.nsmc.org.cn/portalsite/default.aspx>).

#### References

- Atkins, N. T., Wakimoto, R. M., & Ziegler, C. L. (1998). Observations of the finescale structure of a dryline during VORTEX 95. *Monthly Weather Review*, *126*, 525–550.
- Blanchard, D. O. (2008). Interactions between a super-cell and a quasi-stationary frontal boundary. *Monthly Weather Review*, *136*, 5199–5210.
- Bluestein, H. B., McCaul, E. W., Byrd, G. P., & Woodall, G. R. (1988). Mobile sounding observations of a tornadic storm near the dryline: The Canadian, Texas storm of 7 May 1986. *Monthly Weather Review*, *116*, 1790–1804.
- Bryan, G. H., & Fritsch, J. M. (2002). A benchmark simulation for moist nonhydrostatic numerical models. *Monthly Weather Review*, *130*, 2917–2928.
- Campbell, P. C., Geerts, B., & Bergmaier, P. T. (2014). A dryline in southeast Wyoming. Part I: Multiscale analysis using observations and modeling on 22 June 2010. *Monthly Weather Review*, *142*, 268–289.
- Carbone, R. E., Conway, J. W., Crook, N. A., & Moncrieff, M. W. (1990). The generation and propagation of a nocturnal squall line. Part I: Observations and implications for mesoscale predictability. *Monthly Weather Review*, *118*, 26–49.
- Coffer, B. E., Maudlin, L. C., Veals, P. G., & Clark, A. J. (2013). Dryline position errors in experimental convection-Allowing NSSL-WRF model forecasts and the operational NAM. *Weather and Forecasting*, *28*, 746–761.
- Crook, N. A. (1996). Sensitivity of moist convection forced by boundary layer processes to low-level thermodynamic fields. *Monthly Weather Review*, *124*, 1767–1785.
- Droegemeier, K. K., & Wilhelmson, R. B. (1985a). Three-dimensional numerical modeling of convection produced by interacting thunderstorm outflows. Part I: Control simulation and low-level moisture values. *Journal of the Atmospheric Sciences*, *42*, 2381–2403.
- Droegemeier, K. K., & Wilhelmson, R. B. (1985b). Three-dimensional numerical modeling of convection produced by interacting thunderstorm outflows. Part I: Control simulation and low-level moisture variations. *Journal of the Atmospheric Sciences*, *42*, 2404–2414.
- Fovell, R. G., Mullendore, G. L., & Kim, S. (2006). Discrete propagation in numerically simulated nocturnal squall lines. *Monthly Weather Review*, *134*, 3735–3752.
- Friedrich, K., Kingsmill, D. E., & Young, C. R. (2005). Misocyclone characteristics along Florida gust fronts during CaPE. *Monthly Weather Review*, *133*, 3345–3367.
- Geerts, B., Parsons, D., Ziegler, C. L., Weckwerth, T. M., Biggerstaff, M. I., Clark, R. D., et al. (2017). The 2015 Plains Elevated Convection at Night Field Project. *Bulletin of the American Meteorological Society*, *98*(4), 767–786.
- Hane, C. E., Bluestein, H. B., Crawford, T. M., Baldwin, M. E., & Rabin, R. M. (1997). Severe thunderstorm development in relation to along-dryline variability: A case study. *Monthly Weather Review*, *125*, 231–251.
- Harrison, S. J., Mecikalski, J. R., & Knupp, K. R. (2009). Analysis of outflow boundary collisions in north-central Alabama. *Weather and Forecasting*, *24*, 1680–1690.
- He, Z., Zhang, Q., Bai, L., & Meng, Z. (2017). Characteristics of mesoscale convective systems in central East China and their reliance on atmospheric circulation patterns. *International Journal of Climatology*, *37*(7), 3276–3290.
- Hoch, J., & Markowski, P. (2005). A climatology of springtime dryline position in the U.S. Great Plains region. *Journal of Climate*, *18*, 2132–2137.
- Huang, Y., Meng, Z., Li, J., Li, W., Bai, L., Zhang, M., & Wang, X. (2017). Distribution and variability of satellite-derived signals of isolated convection initiation over central eastern China. *Journal of Geophysical Research: Atmospheres*, *122*, 11,357–11,373.
- Intrieri, J. M., Bedard, A. J. Jr., & Hardesty, R. M. (1990). Details of colliding thunderstorm outflows as observed by Doppler lidar. *Journal of the Atmospheric Sciences*, *47*, 1081–1098.
- Kingsmill, D. E. (1995). Convection initiation associated with a sea-breeze front, a gust front, and their collision. *Monthly Weather Review*, *123*, 2913–2933.
- Knight, C. A., & Squires, P. (1982). *Hailstorms of the central high plains: I The national hail research experiment* (p. 282). Boulder, CO: Colorado Associated University Press.
- Koch, S. E., & McCarthy, J. (1982). The evolution of an Oklahoma dryline. Part II: Boundary-layer forcing of mesoconvective systems. *Journal of the Atmospheric Sciences*, *39*, 237–257.
- Lee, B. D., & Wilhelmson, R. B. (1997a). The numerical simulation of non-supercell tornadogenesis. Part I: Initiation and evolution of pre-tornadic misocyclone circulation along a dry outflow boundary. *Journal of the Atmospheric Sciences*, *54*, 32–60.
- Lee, B. D., & Wilhelmson, R. B. (1997b). The numerical simulation of non-supercell tornadogenesis. Part II: Evolution of a family of tornadoes along a weak outflow boundary. *Journal of the Atmospheric Sciences*, *54*, 2387–2415.
- Lock, N. A., & Houston, A. L. (2014). Empirical examination of the factors regulating thunderstorm initiation. *Monthly Weather Review*, *142*, 240–258.
- Markowski, P. M., Hannon, C., & Rasmussen, E. (2006). Observations of convection initiation “failure” from the 12 June 2002 IHOP deployment. *Monthly Weather Review*, *134*, 375–405.
- Markowski, P. M., Straka, J. M., Rasmussen, E. N., & Blanchard, D. O. (1998). Variability of storm-relative helicity during VORTEX. *Monthly Weather Review*, *126*, 2959–2971.
- McCarthy, J., & Koch, S. E. (1982). The evolution of an Oklahoma dryline. Part I: A meso- and subsynoptic-scale analysis. *Journal of the Atmospheric Sciences*, *39*, 225–236.
- Meng, Z., Bai, L., Zhang, M., Wu, Z., Li, Z., Pu, M., et al. (2018). The deadliest tornado (EF4) in the past 40 years in China. *Weather and Forecasting*, *33*, 693–713.
- Meng, Z., Yan, D., & Zhang, Y. (2013). General features of squall lines in East China. *Monthly Weather Review*, *141*, 1629–1647.
- Niu, S., Zhang, Y., Xi, S., Liu, W., & Liang, J. (2012). Analysis on the formation mechanism of a strong squall line based on intensive observation data in Shangqiu on 3 June, 2009 (in Chinese). *Torrential Rain and Disasters*, *31*, 255–263.
- Peters, K., & Hohenegger, C. (2017). On the dependence of squall-line characteristics on surface conditions. *Journal of the Atmospheric Sciences*, *74*, 2211–2228.
- Potvin, C. K., Elmore, K. L., & Weiss, S. J. (2010). Assessing the impacts of proximity sounding criteria on the climatology of significant tornado environments. *Weather and Forecasting*, *25*, 921–930.

- Purdom, J. F. W. (1976). Some uses of high-resolution GOES imagery in the mesoscale forecasting of convection and its behavior. *Monthly Weather Review*, *104*, 1474–1483.
- Purdom, J. F. W. (1982). Subjective interpretation of geostationary satellite data for nowcasting. In K. Browning (Ed.), *Nowcasting* (pp. 149–166). San Diego, CA: Academic Press.
- Qin, R., & Chen, M. (2017). Impact of a front–dryline merger on convection initiation near a mountain ridge in Beijing. *Monthly Weather Review*, *145*, 2611–2633.
- Schumacher, R. S. (2015). Resolution dependence of initiation and upscale growth of deep convection in convection-allowing forecasts of the 31 May–1 June 2013 supercell and MCS. *Monthly Weather Review*, *143*, 4331–4354.
- Stonitsch, J. R., & Markowski, P. M. (2007). Unusually long duration, multiple-Doppler radar observations of a front in a convective boundary layer. *Monthly Weather Review*, *135*, 93–117.
- Su, T., & Zhai, G. (2017). The role of convectively generated gravity waves on convective initiation: A case study. *Monthly Weather Review*, *145*, 335–359.
- Taylor, N. M., Sills, D. M. L., Hanesiak, J. M., Milbrandt, J. A., Smith, C. D., Strong, G. S., et al. (2011). The understanding severe thunderstorms and Alberta boundary layers experiment (UNSTABLE) 2008. *Bulletin of the American Meteorological Society*, *92*, 739–763.
- Trier, S. B., Romine, G. S., Ahijevych, D. A., Trapp, R. J., Schumacher, R. S., Coniglio, M. C., & Stensrud, D. J. (2015). Mesoscale thermodynamic influences on convection initiation near a surface dryline in a convection-permitting ensemble. *Monthly Weather Review*, *143*, 3726–3753.
- Wakimoto, R. M., & Murphey, H. V. (2010). Analysis of convergence boundaries observed during IHOP\_2002. *Monthly Weather Review*, *138*, 2737–2760.
- Wakimoto, R. M., Murphey, H. V., Browell, E. V., & Ismail, S. (2006). The “Triple Point” on 24 May 2002 during IHOP. Part I: Airborne Doppler and LASE analyses of the frontal boundaries and convection initiation. *Monthly Weather Review*, *134*, 231–250.
- Weckwerth, T. M. (2000). The effect of small-scale moisture variability on thunderstorm initiation. *Monthly Weather Review*, *128*, 4017–4030.
- Weckwerth, T. M., Parsons, D. B., Koch, S. E., Moore, J. A., LeMone, M. A., Demoz, B. B., et al. (2004). An overview of the International H<sub>2</sub>O Project (IHOP\_2002) and some preliminary highlights. *Bulletin of the American Meteorological Society*, *85*, 253–278.
- Weckwerth, T. M., Murphey, H. V., Flamant, C., Goldstein, J., & Pette, C. R. (2008). An observational study of convection initiation on 12 June 2002 during IHOP\_2002. *Monthly Weather Review*, *136*, 2283–2304.
- Weckwerth, T. M., & Parsons, D. B. (2006). A review of convection initiation and motivation for IHOP\_2002. *Monthly Weather Review*, *134*, 5–22.
- Weiss, C. C., & Bluestein, H. B. (2002). Airborne pseudo-dual Doppler analysis of a dryline–outflow boundary intersection. *Monthly Weather Review*, *130*, 1207–1226.
- Wilson, J. W., & Meigenhardt, D. L. (1997). Thunderstorm initiation, organization, and lifetime associated with Florida boundary layer convergence lines. *Monthly Weather Review*, *125*, 1508–1525.
- Wilson, J. W., Moore, J. A., Foote, G. B., Martner, B., Rodi, A. R., Uttal, T., & Wilczak, J. M. (1988). Convection initiation and downburst experiment (CINDE). *Bulletin of the American Meteorological Society*, *69*, 1328–1348.
- Wilson, J. W., & Roberts, R. (2003). Predictability of convective storm initiation. 31st International Conference on Radar Meteorology, Seattle, WA, Amer. Meteor. Soc., 12A.1. Retrieved from <https://ams.confex.com/ams/32BC31R5C/webprogram/Paper64219.html>
- Wilson, J. W., & Roberts, R. (2006). Summary of convective storm initiation and evolution during IHOP: Observational and modeling perspective. *Monthly Weather Review*, *134*, 23–47.
- Wilson, J. W., & Schreiber, W. E. (1986). Initiation of convective storms at radar-observed boundary-layer convergence lines. *Monthly Weather Review*, *114*, 2516–2536.
- WSEC (2006). A recommendation for an enhanced Fujita scale (EF-scale). Texas Tech University Wind Science and Engineering Center Rep. (111 pp.). Retrieved from [www.depts.ttu.edu/nwi/Pubs/FScale/EFScale.pdf](http://www.depts.ttu.edu/nwi/Pubs/FScale/EFScale.pdf)
- Wulfmeyer, V., Behrendt, A., Bauer, H., Kottmeier, C., Corsmeier, U., Blyth, A., et al. (2008). Research campaign: The convective and orographically induced precipitation: A research and development project of the World Weather Research Program for improving quantitative precipitation forecasting in low-mountain regions. *Bulletin of the American Meteorological Society*, *89*, 1477–1486.
- Zhang, F., Snyder, C., & Rotunno, R. (2003). Effects of Moist Convection on Mesoscale Predictability. *Journal of the Atmospheric Sciences*, *60*, 1173–1185.
- Zhang, M., Meng, Z., & Huang, Y. (2019). The mechanism and predictability of an elevated convection initiation event in a weak-lifting environment in central eastern China. *Monthly Weather Review*. Accepted upon minor revision
- Zhang, Y., Ding, Z., & Huang, X. (2012). Analysis on formation reason of a squall line weather in the Yellow River and Huaihe River basins. *Meteorological and Environmental Research*, *9*, 11–14.
- Zhang, Y., Zhang, F., Stensrud, D. J., & Meng, Z. (2016). Intrinsic predictability of the 20 May 2013 tornadic thunderstorm event in Oklahoma at storm scales. *Monthly Weather Review*, *144*, 1273–1298.
- Zhu, X., & Zhu, J. (2004). New generation weather radar network in China (in Chinese). *Meteorological Science and Technology*, *32*, 255–258.
- Zhuge, X., Yu, F., & Zhang, C. (2011). Rainfall retrieval and nowcasting based on multispectral satellite images. Part I: Retrieval study on daytime 10-minute rain rate. *Journal of Hydrometeorology*, *12*, 1255–1270.
- Ziegler, C. L. (2014). Deep convection initiation: State of the science, limits of understanding, and future directions. Preprints, 94th American Meteorological Society Annual Meeting, Atlanta, GA, Amer. Meteor. Soc., 1.3. Retrieved from <https://ams.confex.com/ams/94Annual/webprogram/Paper236651.html>
- Ziegler, C. L., Lee, T. J., & Pielke, R. A. (1997). Convective initiation at the dryline: A modeling study. *Monthly Weather Review*, *125*, 1001–1026.
- Ziegler, C. L., & Rasmussen, E. N. (1998). The initiation of moist convection at the dryline: Forecasting issues from a case study perspective. *Weather and Forecasting*, *13*, 1106–1131.